Chapter

Diluted Magnetic Semiconductors Nanocrystals: Saturation and Modulation

Anielle C.A. Silva, Amanda I.S. Barbosa, Alessandra S. Silva, Elisson A. Batista, Thaís K. de Lima Rezende, Éder V. Guimarães, Ricardo S. Silva and Noelio O. Dantas

Abstract

Diluted Magnetic Semiconductor (DMS) nanocrystals are a new class of materials formed by doping the semiconductor with transition metals (TM), which gives interesting magneto-optical properties. These properties are attributed to the exchange interaction between the pure semiconductor's sp-electrons and the localized TM d-electrons. This book chapter shows exciting results of new DMS developed by the group, both in powder form and embedded in glassy systems. Depending on the concentration of doping ions, saturation of the incorporation of substitutional and interstitial sites in the nanocrystal structure may occur, forming other nanocrystals. In this context, we investigated the doping saturation limit in nanopowders of DMS $Zn_{1-x}Mn_xO$ NCs and $Zn_{1-x}Mn_xTe$, $Zn_{0.99-x}Mn_{0.01}Co_xTe$, and $Bi_{2-x}Co_xS$ NCs synthesized in glassy matrices. Thus, the sites' saturation into the crystalline lattice of nanocrystals is a topic little reported in the literature, and we will comment on this work. Therefore, we will show results from the group about the modulation and saturation in diluted magnetic semiconductors nanocrystals in this work.

Keywords: Diluted magnetic semiconductor, Nanocrystals, Saturation, Modulation, Doping, Transition metal

1. Introduction

The doping of semiconductors with small concentrations of transition metals (TM) ions, such as Co^{2+}, Cr^{3+}, Fe^{3+}, Mn^{2+}, allows the formation of new types of materials that have interesting spin-dependent electrical, optical, magnetic, and structural properties [1–3]. These new properties are attributed to the sp-d exchange interactions that involve the d-sub-levels of transition metal (TM) ions and the sp-electrons of the conduction band and/or holes in the host semiconductor valence band [4, 5]. These materials are called diluted magnetic semiconductors (DMS) and present great possibilities for technological applications such as the production of light-emitting diodes (LEDs) [6], spin transistors [7], lasers [8], supercapacitor [9], among others.

DMS materials, when developed under the quantum confinement regime, form nanocrystals (NCs) with smaller dimensions than the bulk material [10]. These DMS NCs have chemistry and physical properties dependent on their shape and size. These materials are obtained from a controlled process known as thermal diffusion of precursor ions to form DMS NC under the requirement of thermodynamic equilibrium.

The substitutional and interstitial sites' saturation in the nanocrystals structure may occur depending on the dopant concentration, and other nanocrystals types are formed. This system is called a nanocomposite and can have several exciting physical, chemical, and biological properties [11].

In this context, we investigated the doping saturation limit in nanopowders of DMS $Zn_{1-x}Mn_xO$ NCs [12] and $Zn_{1-x}Mn_xTe$ [13], $Zn_{0.99-x}Mn_{0.01}Co_xTe$ [14], and $Bi_{2-x}Co_xS$ [15] NCs synthesized in glassy matrices by the fusion method. The properties of the nanomaterials were investigated by experimental techniques of photoluminescence (PL), UV–Vis spectroscopy, X-ray diffraction (XRD), scanning electron microscopy (SEM), and transmission electron microscopy (MET). The theoretical study applying the crystalline field theory and Uv–Vis spectroscopy data allows identifying the tetrahedral (Th) or octahedral (Oh) location that the TM ions occupy in the crystalline structure of the semiconductor nanocrystal.

2. Diluted magnetic semiconductors in Nanopowders and embedded in glassy matrices

2.1 Synthesis of Nanopowders and nanocrystals and embedded in glassy matrices

ZnO NCs were synthesized by precipitation method using zinc nitrate and sodium hydroxide (NaOH, ≥98%) as precursors. In this work, the aqueous solution (1 M) of zinc nitrate (Zn(NO3)2. 6H2O, 98%) and the solution (2 M) of NaOH were mixed at room temperature. The NaOH solution was slowly added into zinc nitrate solution under vigorous stirring, which resulted in the formation of a white suspension. The white product was centrifuged at 6000 rpm for 5 min and washed several times with distilled water until the pH of the solution is around 7. The obtained samples were dried at 100°C for 24 hours. The samples were not subjected to temperatures above 100oC to avoid diffusion of Mn2+ ions from the nucleus to the surface of the ZnO NCs [15], since this is not the focus of this work. The ZnO:x Mn NCs were synthesized using the same procedure as ZnO NCs, but with the manganese (II) chloride (MnCl2, 98%) solution during the synthesis process. The xMn- concentration was determined based on the mass percentage of Zn present in ZnO (wt%), for x = 0.1; 0.3; 0.5; 0.7; 0.9; 1.0; 3.0; 5.0; 7.0 and 9.0. All reagents are nearly pure and purchased from Sigma-Aldrich Company.

$Zn_{1-x}Mn_xTe$ and $Zn_{0.99-x}Mn_{0.01}Co_xTe$ were synthesized by fusion method in a glass matrix and annealed post-growth. The fusion method consists of two sequential melting-nucleation processes that produce ensembles of nearly spherical nanoparticles embedded in a glass matrix. In the first step, the PZABP glass matrix with a nominal composition of $65P_2O_5 \cdot 14ZnO \cdot 1Al_2O_3 \cdot 10BaO \cdot 10PbO$ (mol %) adding 2Te (wt %), and Mn and/or Co at doping *x* content varying with Zn content from 0 to 80 (wt %), were synthesized by fusion in alumina crucibles at 1300°C for 30 minutes. Next, these melted mixtures were quickly cooled to room temperature forming a glass system doped with the precursor ions needed for nanoparticle growth. In the second step, the glass samples were thermally annealed at 500°C

for 10 hours to enhance the diffusion of Zn^{2+}, Mn^{2+} and/or Co^{2+} and Te^{2-} ions throughout the host PZABP matrix and induce the growth of $Zn_{1-x}Mn_xTe/Zn_{0.99-x}Mn_{0.01}Co_xTe$ NCs. The physical properties of the glass samples were studied by optical absorption (OA), recorded with a model UV-3600 Shimadzu UV–VIS–NIR spectrometer, operating between 190 and 3300 nm; Photoluminescence (PL), using a 405 nm (~ 3.06 eV) continuous wave laser; Transmission electron micrographs (TEM JOEL, JEM-2100, 200 kV) and electron paramagnetic resonance (EPR), using a high sensitivity Bruker ESP-300 spectrometer (operating at X-band ~9.75 GHz and at Q-band ~34GHz).

Co^{2+}-doped Bi_2S_3 NCs were synthesized in a glass matrix with nominal composition of $45SiO_2$. $30Na_2CO_3$.$1Al_2O_3$. $24B_2O_3$ (mol%) adding 2S (wt%), 2Bi (wt%) and x = 0, 1 and 5% of Cobalt (Co), as a function of Bismuth (Bi) concentration. Samples were produced with the powder mixture added in an alumina crucible, and placed in a furnace at 1200 C for 30 min, followed by a fast cooling of the melted mixture down to room temperature, which formed a host glass. Thermal annealing was the next step: The previously-melted glass matrix, as-growth, was then heated at 500 C for 2, 10 and 24 h to enhance the diffusion of Bi^{3+} Co^{2+}, and S^{2-} ions precursors within the hosting matrix, resulting in the formation of DMS $Bi_{2-x}Co_xS_3$ NCs.

2.2 A study in function of Mn concentration in ZnO nanocrystals: Solubility and Mn^{2+} ions localization

The zinc oxide (ZnO) is a semiconductor with several interesting physical and biological properties such as ultraviolet absorption and bactericidal and antitumor properties [16]. Depending on the ions incorporated in the crystalline structure of ZnO nanocrystals (NCs) one can intensify or generate new and interesting properties. Dantas et al. demonstrated that doped ZnO nanocrystals' bactericidal and antitumor properties are potentiated or inhibited with the concentration and type of dopant [17]. The ZnO is a semiconductor of family II-VI that has a bandgap of 3.44 eV [18]. Due to its wide bandgap range, ZnO is suitable for technological applications of photonic devices operating in the blue and ultraviolet region, fabrication of nanodevices electronics [16, 19].

The structural and optical properties are shown in **Figure 1**. The characteristic diffraction patterns of ZnO crystals with wurtzite structure (JCPDS n° 36–1451) were observed in the X-ray patterns of samples (**Figure 1a**). The presence of additional diffraction peaks for concentrations above 3.0 Mn (%wt) corresponding to the phase $ZnMn_2O_4$ (JCPDS n° 24–1133), indicating the formation of the second phase (open circles). The closed circles are identified by the aluminum sample holder. Thus, this new crystal formation is associated with the saturation of the substitutional and interstitial sites in the ZnO crystal structure.

In order to identify the symmetrical environment in which the Mn^{2+} ions may be found in the ZnO NCs, adjustments will be made to the optical absorption spectra of the samples (ZnO, 0.5Mn, 1.0Mn and 9Mn) shown in **Figure 1(b)**. These adjustments are made in the positions of absorption of Mn^{2+} ions, making possible the use of the crystalline field theory (CFT) based on the crystalline field strength parameters Δ and Racah B, both calculated with help of Tanabe– Sugano diagram (**Figure 1(c)**) [20]. From the OA spectra of the NCs of Zn: xMn, based on the Tanabe-Sugano diagram, the energies of the characteristic electronic transitions of Mn^{2+}: $^6A_1$ (^6S) → $^4T_1$ (^4G) (691 nm), $^6A_1$ (^6S) → $^4T_2$ (^4G) (590 nm), $^6A_1$ (^6S) → $^4T_2$ (^4D) (482 nm), and $^6A_1$ (^6S) → ^2E (^2I) (410 nm) (**Figure 1b**) subtly permitted by spin-orbit coupling were effectively described by the Racah B parameter (559 cm^{-1}) and the crystalline field division (Δ = 5464 cm^{-1}) [21, 22].

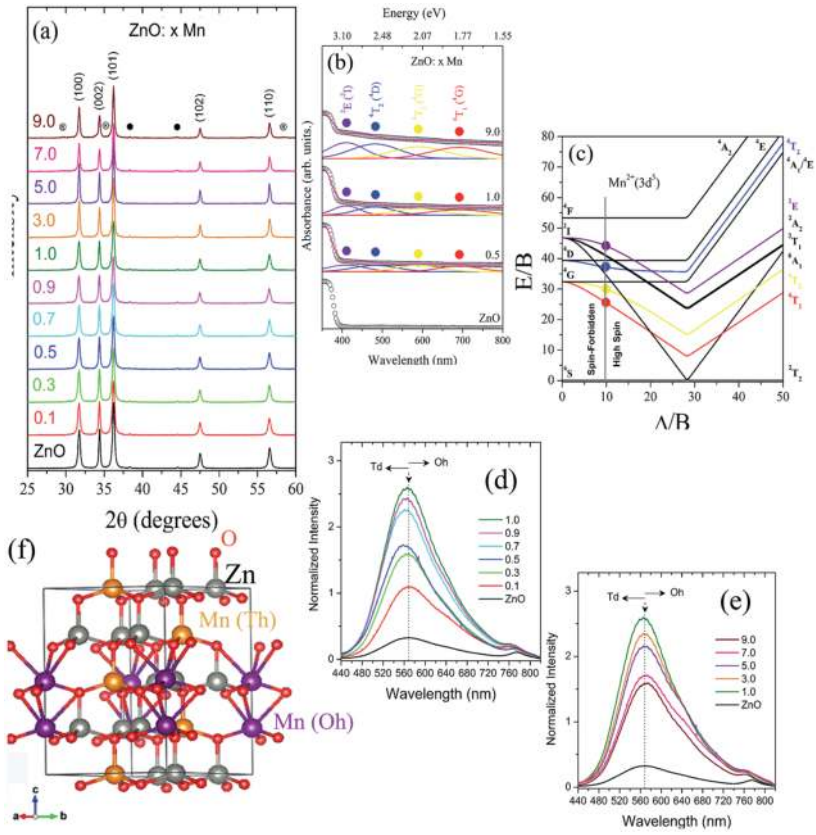

Figure 1.
(a) X-ray diffractograms (b) As adjusted curves represent the experimental energies of the transitions prohibited by spin $^6A_1$ (S) → $^4T_1$ (G), $^4T_2$ (G), $^4T_2$ (D), $^2A_2$ (I) e ^2E(I). (c) Tanabe-Sugano diagram for the electronic configuration of the Mn2+ (3d5) (C/B = 4.5) with vertical solid line in Δ/B = 9.77, Δ = 5464 cm^{-1}, and B = 559 cm^{-1}, PL spectra from 440 to 820 nm for concentrations of (d) 0.1 to 1.0 of Mn and (e) of 1.0 to 9.0 of Mn, (f) wurtzite structure of ZnO NCs with coordination geometry in which the Mn^{2+} ions are, represented by tetrahedral sites (td) and octahedral sites (od).

The results from Δ and B show that the Mn^{2+} dopants incorporated mainly at octahedral sites in the hexagonal structure of ZnO, for the sample with low concentration, and in the tetragonal structure of $ZnMn_2O_4$. Thus, the excited states of the Mn^{2+} in the binder field reside in the host semiconductor energy gap [21, 22].

Fluorescence spectra of the nanocrystals of ZnO: x Mn where the band at 570 nm are assigned to vacancies [23] are shown in **Figure 1(d, e)**. Luminescence intensification and *blue shift* to a concentration of 0.5 Mn. This result confirms the incorporation of Mn^{+2} ions into the tetrahedral sites of ZnO NCs (inside nanocrystal). However, there is a contribution to incorporating Mn^{2+} ions into the octahedral sites (surface nanocrystal). It is noteworthy that the band widening around 570 nm is due an overlapping characteristics bands of oxygen vacancies and d–d ($^4T_1 \leftarrow {}^6A_1$) of Mn^{2+}-ions in ZnO NC host [23, 24].

As the concentration increases from 0.5 to 1.0 Mn, the band's position remains, confirmed the half-height with x_{Mn}-concentration, which is related to the presence of the formation of the $ZnMn_2O_4$ NCs and that the Mn^{2+} are incorporated in the octahedral sites of the crystal structure saturation of the sites present in the ZnO NCs.

In order to visually check how these are coordination geometry, **Figure 1(f)** shows the wurtzite structure of ZnO NCs, which the Mn^{2+} ions are in tetrahedral sites (Td) and/or octahedral sites (Od).

2.3 Solubility of manganese and cobalt in ZnTe nanocrystals embedded in P_2O_5 - ZnO - Al_2O_3 - BaO - PbO glassy matrix

The incorporation of magnetic ions into the crystal structure of ZnTe semiconductor nanocrystals, which grow in glassy systems, has become very interesting due to the various applications in spintronics are governed by sp–d spin interaction between carriers and magnetic ions [25]. Some possible applications require nanoparticles to be embedded in highly stable, robust, and transparent host materials, as glassy systems [26]. The present study reports on the investigation of the solubility/saturation of Mn^{2+} ions in $Zn_{1-x}Mn_xTe$ [13, 26, 27] and competition between Co^{2+} and Mn^{2+} ions into $Zn_{0.99-x}Mn_{0.01}Co_xTe$ [14, 28] nanosized DMS embedded in a glassy system with a wider Mn/Co concentration range (x = 0.000–0.800). According to the literature, the Mn^{2+}/Co^{2+} ion can be thermodynamically incorporated into II-VI semiconductors up to its solubility limit [29, 30]. Above this limit, saturation occurs, and Mn^{2+}/Co^{2+} ions tend to be expelled toward the semiconductor nanocrystal surface [30].

Figure 2 presents OA (a) and PL (c) spectra and photographs (b) of the samples containing $Zn_{1-}xMn_xTe$ NCs, with Mn-concentrations ranging from x = 0.000 to x = 0.800, and with PZABP ($65P_2O_5 \cdot 14ZnO \cdot 1Al_2O_3 \cdot 10BaO \cdot 10PbO$ (mol %)) glassy matrix doped only 80Mn (% wt of Zn). The OA spectra show absorption bands centered attributed to $Zn_{1-}xMn_xTe$ NCs (quantum dots (QDs) and bulk NCs) and the incorporation of Mn^{2+} ions. This substitutional incorporation is confirmed from the EPR spectra (**Figure 2(f)**) that showed six lines associated to S = 5/2 spin half-filled d-state, characteristic of Mn^{2+} ions (as detailed in the energy diagram) [26]. For x > 0, additional bands are observed.

The absorption band centered at 3.54 eV is attributed at MnO_2, and the bands centered at 3.02, and 2.43 eV is attributed at MnO [31]. The TEM images in **Figure 2(e)** (for x = 0.100), revealed interplanar distances corresponding to $Zn_{0.9}Mn_{0.1}Te$ NCs (d ~ 0.347 nm) [32], MnO (d ~ 0.224 nm) [33] and MnO_2 (d ~ 0.582 nm) NCs [34]. This result can be confirmed by the PL spectra, on what the observed redshift shows that it was possible to tune Mn emission energy from orange to near-infrared as a function of concentration. These results confirm the successful inclusion of Mn^{2+} ions in the $Zn_{1-}xMn_xTe$ up to the nominal solubility limit of x = 0.100. Above this solubility limit, one can observe Mn′s saturation, forming MnO and MnO_2 NCs, as represented in **Figure 2(d)**. Thus, one of the main motivations for studying semiconductors doped with transition metals, especially Mn^{2+} ions, is for applications in luminescent devices.

Figure 3 presents OA (a), PL (b) and EPR (c) spectra and photographs (between OA and PL spectra) of the samples containing $Zn_{0.99-x}Mn_{0.01}Co_xTe$ NCs, with Co-concentrations ranging from x = 0.000 to x = 0.800. **Figure 3(d)** presents the energy diagram of all transitions related to OA and PL data, and **Figure 3(e)** shows the transitions satisfying the selection rules $\Delta M_S = \pm 1$ and $\Delta M_I = 0$. The AO spectra, besides the bands attributed to $Zn_{1-}xMn_xTe$ QDs and bulk NCs, as previously presented in **Figure 3**, four characteristic bands in the visible spectrum for all doped samples with cobalt. These four are due to the spin-allowed transitions: $^4A_2(F) \rightarrow {}^2T_1(P)$ (2.13 eV); and spin-forbidden transitions: $^4A_2(F) \rightarrow {}^2A_1(G)$ (2.33 eV), $^4A_2(F) \rightarrow {}^4T_1(G)$ (1.95 eV) and $^4A_2(F) \rightarrow {}^2E(G)$ (1.91 eV) [14]. These bands show the substitutional incorporation of Co^{2+} ions in tetrahedral Zn^{2+} ions sites. The PL spectra show emissions from two NC groups: QDs (E_{exc} ~ 2.53 eV) and bulk NCs (E_b ~ 2.21 eV); defects related to zinc vacancies (E_{VZn} ~ 2.53 eV) and oxygen centers (E_o ~ 1.91 eV) [14, 27].

The emission centered at approximately 2.03 eV and 1.89 eV corresponds to tetrahedrally (Td) and octahedrally (Oh) coordinated Mn^{2+} ions. Already, when the

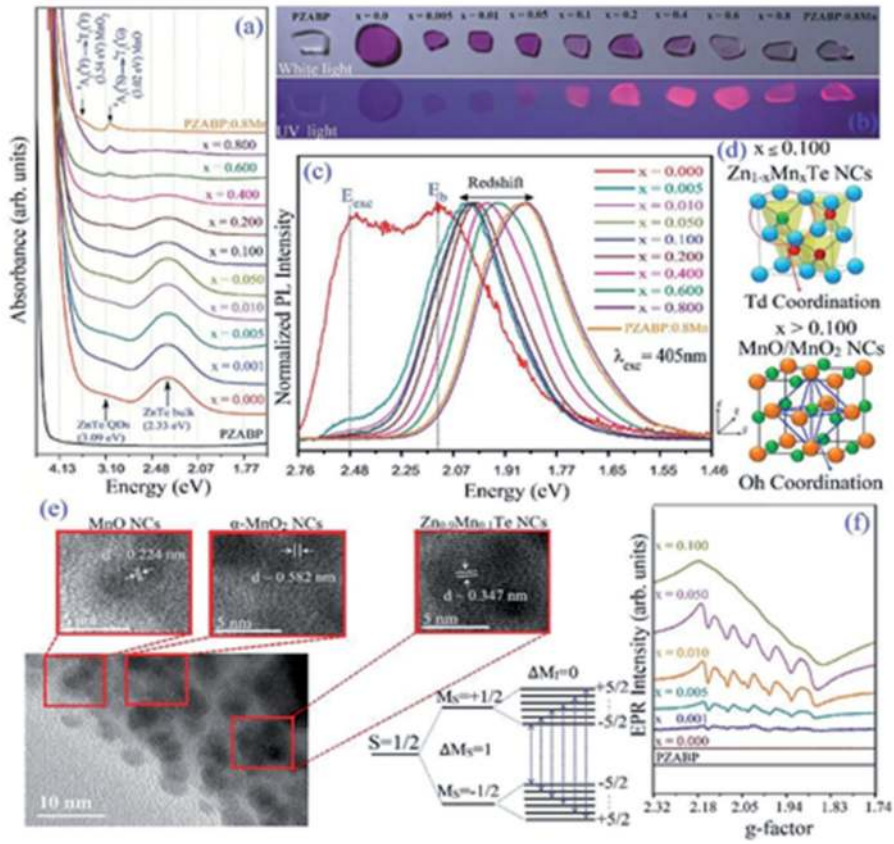

Figure 2.
OA (a) and PL (c) spectra and photographs (b) of samples containing $Zn_{1-x}Mn_xTe$ NCs, with Mn-concentrations ranging from x = 0.000 to x = 0.800. In (d) Mn^{2+} ions located in tetrahedral sites (td) of ZnTe NCs (concentration x < 0.100) and Mn^{2+} and Mn^{4+} located in octahedral sites (oh) of MnO and MnO_2 NCs (concentration x ≥ 0.100); (e) TEM images for concentration x = 0.100; (f) EPR spectra of $Zn_{1-x}Mn_xTe$ NCs with Mn concentrations varying from x = 0.00 to x = 0.100 and selection rules $\Delta M_S = \pm 1$ and $\Delta M_I = 0$ (next to).

spin-allowed transitions centred around 1.69 eV ($^4T_1(^4P) \rightarrow {}^4A_2(^4F)$, named E_{1Co2+}) and 1.52 eV ($^4T_1(^4P) \rightarrow {}^4T_2(^4F)$, named E_{2Co2+}) [14]. The energy diagram in **Figure 3(d)** shows these OA and PL spectra transitions. The EPR spectra, besides proving the substitutional incorporation of Mn^{2+} in $Zn_{1-x}Mn_xTe$, as justified by **Figure 3(f)**, also reveals that as the Co doping, an intense central line with g = 2.012 attributed to interacting Co^{2+} [14]. For both Mn^{2+} and Co^{2+} ions the transitions observed satisfy the selection rules $\Delta M_S = \pm 1$ and $\Delta M_I = 0$ (**Figure 3(e)**). Thus, the EPR spectra suggest a kind of competition between Mn^{2+} and Co^{2+} ions to substitute Zn^{2+} ions, controlled by the Co concentration.

2.4 Effects of symmetry and concentration of cobalt-doped Bi_2S_3 nanocrystals embedded in host glass matrix

Bi_2S_3 semiconductor nanocrystals (NCs) present radioactive recombination of electron–hole carriers adjustable according to the temperature, time, and concentration of doping ions in the system [15, 35–37]. The occupation of vacancies in the Bi_2S_3 orthorhombic network by Co^{2+} ions (0.72 Å) replacing Bi^{3+} ions (1.03 Å) can reduce intrinsic point defects and consequently increase the efficiency of semiconductor nanocrystals, for applications in solar cells [38], photocatalytic devices of visible light [39], thermoelectric [40] and spintronic [41]. Therefore, the control of the magnetic saturation of the energy states located of the Co^{2+} ions in the Bi_2S_3 NCs

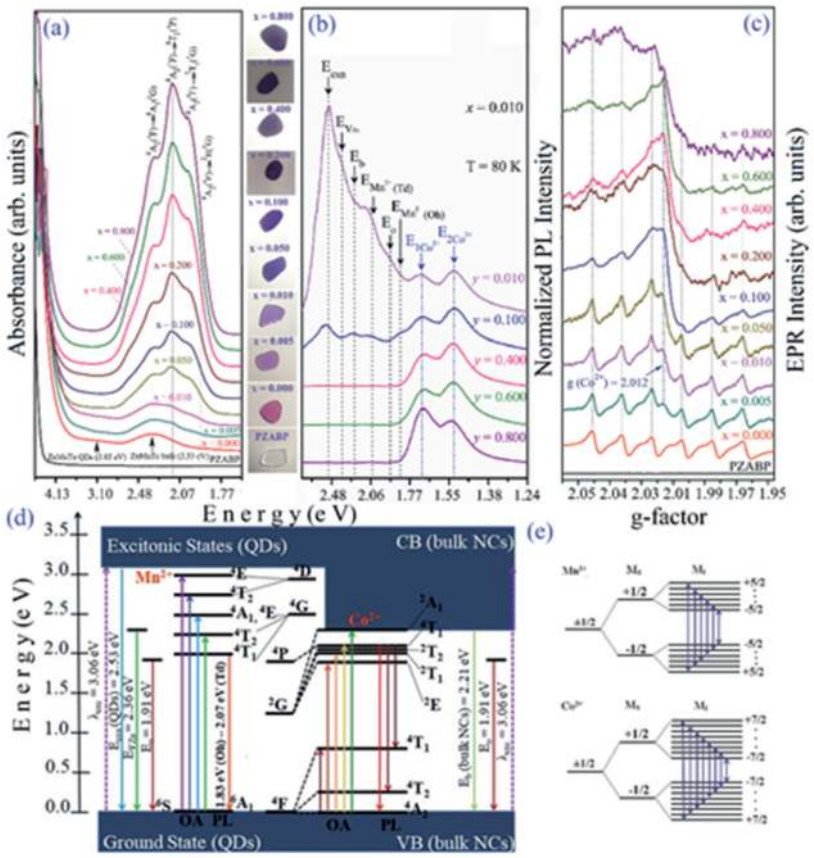

Figure 3.
OA (a), PL (b) and EPR (c) spectra and photographs (between OA and PL spectra) of the samples containing $Zn_{0.99-x}Mn_{0.01}Co_xTe$ NCs, with Co-concentrations ranging from x = 0.000 to x = 0.800. Energy diagram of all transitions related to OA and PL data (d). Transitions satisfying the Mn^{2+} and Co^{2+} selection rules $\Delta M_S = \pm 1$ and $\Delta M_I = 0$ (e).

bandgap allows assigning new magnetic and optoelectronic properties. In this context, we investigated the effect of the molar fraction and the coordination symmetry of Co^{2+} ions in cobalt-doped Bi_2S_3 NCs embedded in a host glass matrix (SNAB - $45SiO_2 \cdot 30Na_2CO_3 \cdot 5Al_2O_3 \cdot 20B_2O_3$) (mol%).

Figure 4(a) shows the UV–VIS–NIR optical absorption spectrum (OA) of the $Bi_{2-x}Co_xS_3$ NCs embedded in a SNAB glass matrix, at temperature (300 K), as a function of the increasing concentration of doping xCo ions (x = 0.000; 0.005; 0.010; 0.050; 0.100). The OA spectrum of the SNAB matrix is transparent in the spectral region where the $Bi_{2-x}Co_xS_3$ NCs can absorb and emit a photon. The OA spectrum of the samples shows energy bands of the exciton charge carrying states and the d-d transitions of the Co^{2+} ions in the $Bi_{2-x}Co_xS_3$ NCs. The structure of the absorption bands is due to that of the ligand field of S^{2-} ions in distorted tetrahedral sites around the Co^{2+} ions. Such bands of electronic level transitions have increased due to the increasing concentration of Co^{2+} ions in the Bi_2S_3 NCs structure.

Furthermore, the p-d and spin-orbit interactions in an asymmetric tetrahedral coordination complex $[CoS_4]^{6-}$ provide a higher intensity for 3d-3d transitions [14, 15, 20, 42]. Therefore, the exotic properties of these new materials called diluted magnetic semiconductors (DMS) NCs are linked to the nature of the sp-d exchange interaction that occurs between the charge carriers of the Bi_2S_3 semiconductor bands around the electrons in the central metal ion orbital (Co^{2+}) with $3d^7$ electronic configuration (spin) $3d^7$ (S = 3/2) [15, 20, 36, 42].

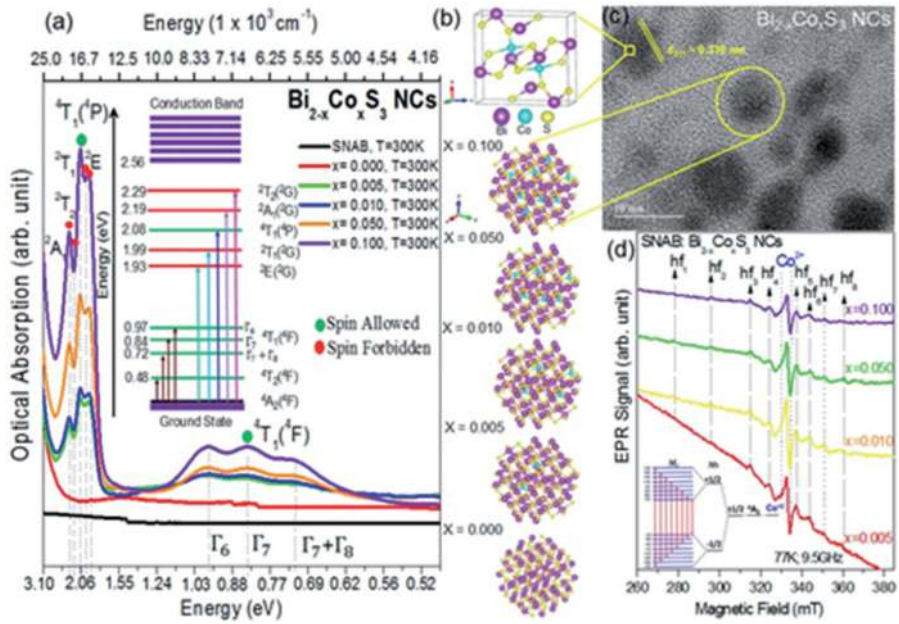

Figure 4.
(a) Optical absorption spectra at room temperature of $Bi_{2-x}Co_xS_3$ NCs (x = 0.000; 0.005; 0.010; 0.050; 0.100) embedded in the SNAB glass matrix annealed for 2 h at 500°C. for comparison purposes, the absorption spectrum of the SNAB glass matrix is represented on the black bottom line. The inset shows the energy level diagram for Co^{2+} ($3d^7$) in a tetrahedral site and the respective spin allowed and forbidden transitions. (b) Bi_2S_3 orthorhombic unit cell and $Bi_{2-x}Co_xS_3$ quantum dots with the interstitial replacement of Bi^{3+} ions by Co^{2+} at distorted tetrahedral sites. (c) TEM image of $Bi_{2-x}Co_xS_3$ NCs (x = 0.100). (d) EPR spectra (77 K) of $Bi_{2-x}Co_xS_3$ NCs (x = 0.005; 0.010; 0.050; 0.100) embedded in the SNAB glass matrix.

For $Bi_{2-x}Co_xS_3$ NCs, the spin allowed transitions $^4A_2$ (^4F) → $^4T_1$ (^4F) and $^4A_2$ (^4F) → $^4T_1$ (^4P) are obtained with the energy value of the barycenter for a normal distribution of the bands observed in the spectrum absorption in the range of 0.62–1.24 eV and 1.70–2.60 eV. The bands observed in the OA spectrum of **Figure 4(a)** correspond to the spin allowed and forbidden transitions, $^4A_2$ (^4F) → $^4T_1$ (^4F) (0.84 eV), $^4A_2$(^4F) → ^2E (^2G) (1.93 eV), $^4A_2$(^4F) → $^2T_1$(^2G) (1.99 eV), $^4A_2$(^4F) → $^4T_1$(^4P) (2.08 e V), $^4A_2$(^4F) → $^2A_1$(^2G) (2.19 eV) and $^4A_2$(^4F) → $^2T_2$(^2G) (2.29 eV). Such identified 3d-3d transitions are attributed to the crystal field strength (Δ = 3882 cm^{-1}) and the electronic repulsion parameter (Racah, B = 772 cm^{-1}), based on the crystal field theory and the Tanabe-Sugano diagram d^7, tetrahedral for C/B = 4.5 [20, 43, 44]. The wide absorption band in the infrared is due to a spin-orbit coupling interaction that split the excited state $^4T_1$ (^4F) into three energy sub-states: $\tilde{A}_6$ (0.97 eV), $\tilde{A}_7$ (0.84 eV) e $\tilde{A}_7 + \tilde{A}_8$ (0.72 eV) [12, 13]. Therefore, the excited states of the Co^{2+} ions are located in the energy gap (2.65 eV) of electrons and holes confined between the ground state and the conduction band of the $Bi_{2-x}Co_xS_3$ NCs. The energy level diagram of Co^{2+} ions ($3d^7$) in a ligand field of S^{2-} ions at tetrahedral coordination sites $[CoS_4]^{6-}$ is shown in the inset in Figure x (a). The energy band associated with the spin allowed transition $^4A_2$ (^4F) → $^4T_1$ (^4F) (0.48 eV) does not appear in the OA spectrum (**Figure 4a**) due to the low intensity and energy [15, 43].

The redshift observed at the OA band edge for the $Bi_{2-x}Co_xS_3$ NCs with increasing concentration xCo, from x = 0.000 (2.75 eV) to x = 0.100 (2.56 eV) (see **Figure 4a**), are consequences of sp-d exchange interactions between sp. electrons confined in states of quantum dots and localized states partially filled with 3d electrons of the Co^{2+} ions [10]. No significant changes occur in the quantum size of the $Bi_{2-x}Co_xS_3$ NCs with the incorporation of Co. The TEM image (**Figure 4c**) shows an average size

of 6 nm for $Bi_{2-x}Co_xS_3$ NCs (x = 0.100) with quantum dot properties. The interplanar distance (d_{211} = 0.310 nm) shows the crystal plane (211) characteristic of the orthorhombic structure of the mineral Bismuthinite. **Figure 4(b)** illustrates the Bi_2S_3 orthorhombic structure unit cell doped with Co^{2+} ions at distorted tetrahedral sites and the respective $Bi_{2-x}Co_xS_3$ quantum dots function of the xCo concentration.

Figure 4(d) shows the EPR spectra obtained in the best conditions at 77 K and 9.75 GHz for samples of $Bi_{2-x}Co_xS_3$ NCs embedded in SNAB glass matrix, with xCo concentration ranging from x = 0.005 to 0.100. The intense central signal at ($g \approx 2.005$; $\Delta H \approx 8$ mT) corresponds to free Co^{+2} ions, dispersed in the glass matrix and not incorporated in the Bi_2S_3 NCs [2, 10]. The inset in Figure x (d) presents a diagram with the allowed hyperfine lines $\Delta M_S = \pm 1$ with $\Delta M_I = 0$, related to the transition between the levels of fine interaction $M_S = +½ \leftrightarrow -½$. The anisotropic characteristic of the eight lines (hf_1; hf_2; hf_3; hf_4; hf_5; hf_6; hf_7; hf_8) of the hyperfine interaction between the electron spin (S = 3/2) and the nuclear spin (I = 7/2) and its similar shapes for all xCo concentrations confirms magnetic doping in distorted tetrahedral sites. The result is compatible with a region where there is a large, inhomogeneous crystal field due to the lack of interface between the host glass matrix and the NCs [42].

3. Conclusion

The synthesis and investigation of the DMS NC have allowed the production of new types of materials with possible technological applications in Engineering, Medicine, Environment, Telecommunications, and others. We report the synthesis of the $Zn_{1-x}Mn_xO$ nanopowders and the Bi2-xCoxS3, Zn1-xMnxTe $Zn_{0.99-x}Mn_{0.01}Co_xTe$ NCs in glass by fusion method. The formation of DMS NCs is observed by SEM and MET images. The EPR spectra confirm the incorporation of TR^{2+} ions (Mn^{2+} and Co^{2+}) in the doped nanocrystals' crystalline structure. The optical properties of these materials were investigated by photoluminescence and Uv–Vis spectroscopy techniques, which show the influence of TR^{2+} ions (Mn^{2+} and Co^{2+}) on the visible spectrum, altering the optical absorption and photoluminescence bands of undoped naocrystals. In this work, we hope to contribute significantly to the study of DMS NCs and their possible technological applications for society's benefit.

Author details

Anielle C.A. Silva[1,2*], Amanda I.S. Barbosa[1], Alessandra S. Silva[5], Elisson A. Batista[3], Thaís K. de Lima Rezende[4], Éder V. Guimarães[5], Ricardo S. Silva[5] and Noelio O. Dantas[1]

1 Laboratory of New Nanostructured and Functional Materials, Physics Institute, Federal University of Alagoas, Maceió, AL, Brazil

2 Programa de Pós-Graduação da Rede Nordeste de Biotecnologia (RENORBIO), Federal University of Alagoas, Maceió, AL, Brazil

3 Physics Institute, Federal University of Uberlândia, Uberlândia, MG, Brazil

4 Chemical Institute, Federal University of Uberlândia, Uberlândia, MG, Brazil

5 Institute of Exact, Natural Sciences and Education (ICENE), Department of Physics, Federal University of Triângulo Mineiro, Uberaba, MG, Brazil

*Address all correspondence to: aniellechristineas@gmail.com

IntechOpen

References

[1] Lourenço, S.A.; Dantas, N.O.; Souza, R. On Synthesis, Optical and magnetic Properties of Semimagnetic Nanocrystals Growth in Glass Matrix. Nanomagnetism **2014**, 53-73.

[2] Silva, R.S. da; Neto, E.S. de F.; Dantas, N.O. Optical, Magnetic, and Structural Properties of Semiconductor and Semimagnetic Nanocrystals. In *Nanocrystals - Synthesis, Characterization and Applications*; 2012.

[3] Schulz, H.J. Transition metal impurities in compound semiconductors: Experimental situation - ScienceDirect. Mater. Chem. Phys. **1987**, *16*, 373-384.

[4] Oliveira, N.; Freitas Neto, E.S. De; Da Silv, R.S. Diluted Magnetic Semiconductor Nanocrystals in Glass Matrix. In *Nanocrystals*; 2010.

[5] Cibert, J.; Scalbert, D. Diluted Magnetic Semiconductors: Basic Physics and Optical Properties. In; Springer, Berlin, Heidelberg, 2008; pp. 389-431.

[6] Wang, C.; Yang, F.; Gao, Y. The highly-efficient light-emitting diodes based on transition metal dichalcogenides: From architecture to performance. Nanoscale Adv. 2020, *2*, 4323-4340.

[7] Rai, D.P.; Laref, A.; Shankar, A.; Sandeep; Sakhya, A.P.; Khenata, R.; Thapa, R.K. Spin-induced transition metal (TM) doped SnO2 a dilute magnetic semiconductor (DMS): A first principles study. J. Phys. Chem. Solids **2018**, *120*, 104-108, doi:10.1016/j.jpcs.2018.04.006.

[8] Morandi, O.; Hervieux, P.A.; Manfredi, G. Laser induced ultrafast demagnetization in diluted magnetic semiconductor nanostructures. In Proceedings of the European Physical Journal D; 2009; Vol. 52, pp. 155-158.

[9] Brozek, C.K.; Zhou, D.; Liu, H.; Li, X.; Kittilstved, K.R.; Gamelin, D.R. Soluble Supercapacitors: Large and Reversible Charge Storage in Colloidal Iron-Doped ZnO Nanocrystals. Nano Lett. **2018**, *18*, 3297-3302, doi:10.1021/acs.nanolett.8b01264.

[10] Dantas, N.O.; dos Silva, A.S.; Silva, A.C.A.; de Neto, E.S.F. Scanning probe microscopies of semiconductor and semimagnetic nanocrystals. In *Advances in Laser and Optics Research*; 2015 ISBN 9781634635226.

[11] Silva, A.; Zóia, M.A.P.; Correia, L.I.V.; Azevedo, F.V.P.V.; Paula, A.T. de; Maia, L.P.; Carvalho, L.S. de; Carvalho, L.N.; Costa, M.P.C.; Giaretta, L.C.; et al. Biocompatibility of Doped Semiconductors Nanocrystals and Nanocomposites. In *Cytotoxicity*; InTech, 2018.

[12] Batista, E.A.; Silva, A.C.A.; de Lima, T.K.; Guimarães, E.V.; da Silva, R.S.; Dantas, N.O. Effect of the location of Mn2+ ions in the optical and magnetic properties of ZnO nanocrystals. J. Alloys Compd. **2021**, *850*, 156611, doi:10.1016/j.jallcom.2020.156611.

[13] Silva, A. dos S.; da Silva, S.W.; de Morais, P.C.; Dantas, N.O. Solubility limit of Mn2+ ions in Zn1−xMnxTe nanocrystals grown within an ultraviolet-transparent glass template. *J. Nanoparticle Res.* 2016, *18*.

[14] Silva, A.S.; Lourenço, S.A.; Da Silva, M.A.T.; Da Silva, S.W.; Morais, P.C.; Dantas, N.O. Effect of Co co-doping on the optical properties of ZnTe:Mn nanocrystals. Phys. Chem. Chem. Phys. **2017**, *19*, 1158-1166, doi:10.1039/c6cp05866c.

[15] Guimarães, E. V.; Gonçalves, E.R.; Lourenço, S.A.; Oliveira, L.C.; Baffa, O.; Silva, A.C.A.; Dantas, N.O.; Silva, R.S.

Concentration effect on the optical and magnetic properties of Co2+-doped Bi2S3 semimagnetic nanocrystals growth in glass matrix. J. Alloys Compd. **2018**, *740*, 974-979, doi:10.1016/j.jallcom.2018.01.073.

[16] Borysiewicz, M.A. ZnO as a functional material, a review. Crystals **2019**, *9*, 505, doi:10.3390/cryst9100505.

[17] Silva, A.; Zóia, M.A.P.; Correia, L.I.V.; Azevedo, F.V.P.V.; Paula, A.T. de; Maia, L.P.; Carvalho, L.S. de; Carvalho, L.N.; Costa, M.P.C.; Giaretta, L.C.; et al. Biocompatibility of Doped Semiconductors Nanocrystals and Nanocomposites. In *Cytotoxicity*; InTech, 2018.

[18] Janotti, A.; Van De Walle, C.G. Fundamentals of zinc oxide as a semiconductor. Reports Prog. Phys. **2009**, *72*, 126501, doi:10.1088/0034-4885/72/12/126501.

[19] Mishra, Y.K.; Adelung, R. ZnO tetrapod materials for functional applications. Mater. Today **2018**, *21*, 631-651, doi:10.1016/j.mattod.2017.11.003.

[20] Lourenço, S.A.; Silva, R.S.; Silva, A.C.A.; Dantas, N.O. Structural and Optical Properties of Co2+-Doped PbSe Nanocrystals in Chalcogeneide Glass Matrix. J. Phys. Chem. C **2015**, *119*, 13277-13282, doi:10.1021/acs.jpcc.5b01920.

[21] Silva, A.S.; Lourenço, S.A.; Dantas, N.O. Mn concentration-dependent tuning of Mn2+ d emission of Zn1-xMnxTe nanocrystals grown in a glass system. Phys. Chem. Chem. Phys. **2016**, *18*, 6069-6076, doi:10.1039/c5cp06802a.

[22] Beaulac, R.; Archer, P.I.; Gamelin, D.R. Luminescence in colloidal Mn2+-doped semiconductor nanocrystals. J. Solid State Chem. **2008**, *181*, 1582– 1589, doi:10.1016/j.jssc.2008.05.001.

[23] Romeiro, F.C.; Marinho, J.Z.; A. Silva, A.C.; Cano, N.F.; Dantas, N.O.; Lima, R.C. Photoluminescence and Magnetism in Mn^{2+} -Doped ZnO Nanostructures Grown Rapidly by the Microwave Hydrothermal Method. J. Phys. Chem. C **2013**, *117*, 26222-26227, doi:10.1021/jp408993y.

[24] Neto, E.S.F.; Dantas, N.O.; Neto, N.M.B.; Guedes, I.; Chen, F. Control of luminescence emitted by Cd1-xMnxS nanocrystals in a glass matrix: X concentration and thermal annealing. Nanotechnology **2011**, *22*, doi:10.1088/0957-4484/22/10/105709.

[25] Karan, N.S.; Sarma, D.D.; Kadam, R.M.; Pradhan, N. Doping transition metal (Mn or Cu) ions in semiconductor nanocrystals. J. Phys. Chem. Lett. **2010**, *1*, 2863-2866, doi:10.1021/jz1012164.

[26] Silva, A.S.; Franco, A.; Pelegrini, F.; Dantas, N.O. Paramagnetic behavior at room temperature of Zn1-xMnxTe nanocrystals grown in a phosphate glass matrix by the fusion method. J. Alloys Compd. 2015, *647*, 637-643.

[27] Silva, A.S.; Lourenço, S.A.; Dantas, N.O. Mn concentration-dependent tuning of Mn2+ d emission of Zn1-xMnxTe nanocrystals grown in a glass system. Phys. Chem. Chem. Phys. **2016**, *18*, 6069-6076, doi:10.1039/c5cp06802a.

[28] Silva, A.S.; Pelegrini, F.; Figueiredo, L.C.; De Souza, P.E.N.; Da Silva, S.W.; De Morais, P.C.; Dantas, N.O. Evidence of competition in the incorporation of Co2+ and Mn2+ ions into the structure of ZnTe nanocrystals. RSC Adv. **2016**, *6*, 101226-101234, doi:10.1039/c6ra19189d.

[29] Sayan Bhattacharyya; Zitoun, D.; Estrin, Y.; Moshe, O.; Rich, D.H.; Gedanken, A. A one-step, template-free synthesis, characterization, optical and magnetic properties of Zn1-xMnxTe nanosheets. *Chem. Mater.* **2009**, *21*, 326-335, doi:10.1021/cm8027737.

[30] Erwin, S.C.; Zu, L.; Haftel, M.I.; Efros, A.L.; Kennedy, T.A.; Norris, D.J. Doping semiconductor nanocrystals. Nature **2005**, *436*, 91-94, doi:10.1038/nature03832.

[31] Noginova, N.; Lindsay, W.; Noginov, M.A.; Loutts, G.B.; Mattix, L. Photorefractive effects in Mn-doped YAlO_3. J. Opt. Soc. Am. B **1999**, *16*, 754, doi:10.1364/josab.16.000754.

[32] Lin, Y.W.; Chen, W.J.; Lu, J.Y.; Chang, Y.H.; Liang, C. Te; Chen, Y.F.; Lu, J.Y. Growth and characterization of ZnO/ZnTe core/shell nanowire arrays on transparent conducting oxide glass substrates. Nanoscale Res. Lett. **2012**, *7*, 1-5, doi:10.1186/1556-276X-7-401.

[33] Liu, B.; Hu, X.; Xu, H.; Luo, W.; Sun, Y.; Huang, Y. Encapsulation of MnO Nanocrystals in Electrospun Carbon Nanofibers as High-Performance Anode Materials for Lithium-Ion Batteries. Sci. Rep. **2015**, *4*, 4229, doi:10.1038/srep04229.

[34] Wei, M.; Konishi, Y.; Zhou, H.; Sugihara, H.; Arakawa, H. Synthesis of single-crystal manganese dioxide nanowires by a soft chemical process. Nanotechnology **2005**, *16*, 245-249, doi:10.1088/0957-4484/16/2/011.

[35] Tarachand; Sharma, V.; Bhatt, R.; Ganesan, V.; Okram, G.S. A catalyst-free new polyol method synthesized hot-pressed Cu-doped Bi2S3 nanorods and their thermoelectric properties. *Nano Res.* **2016**, *9*, 3291-3304, doi:10.1007/s12274-016-1207-6.

[36] Guimarães, É. V.; Mikhail, H.D.; Silva, A.C.A.; Dantas, N.O.; Silva, R.S. Investigations of structural and optical properties of Bi2−xCrxS3 nanocrystals embedded in host glass. Mater. Lett. **2020**, *265*, doi:10.1016/j.matlet.2020.127430.

[37] da Silva, R.; Silva, J.; Rocha, V.; Cano, N.; Almeida Silva, A.; Dantas, N. Synthesis Process Controlled of Semimagnetic $Bi_{2-x}Mn_xS_3$ Nanocrystals in a Host Glass Matrix. *J. Phys. Chem. C* *118*, 18730-18735, doi:10.1021/jp5046657.

[38] Han, D.; Du, M.H.; Dai, C.M.; Sun, D.; Chen, S. Influence of defects and dopants on the photovoltaic performance of Bi2S3: First-principles insights. J. Mater. Chem. A **2017**, *5*, 6200-6210, doi:10.1039/c6ta10377d.

[39] Liu, Z.Q.; Huang, W.Y.; Zhang, Y.M.; Tong, Y.X. Facile hydrothermal synthesis of Bi 2S 3 spheres and CuS/Bi 2S 3 composites nanostructures with enhanced visible-light photocatalytic performances. CrystEngComm **2012**, *14*, 8261-8267, doi:10.1039/c2ce26123e.

[40] Biswas, K.; Zhao, L.D.; Kanatzidis, M.G. Tellurium-free thermoelectric: The anisotropic n -type semiconductor Bi 2S 3. Adv. Energy Mater. **2012**, *2*, 634-638, doi:10.1002/aenm.201100775.

[41] Zhao, G.; Deng, Z.; Jin, C. Advances in new generation diluted magnetic semiconductors with independent spin and charge doping. J. Semicond. 2019, *40*.

[42] Freitas Neto, E.S.; Silva, A.C.A.; da Silva, S.W.; Morais, P.C.; Gómez, J.A.; Baffa, O.; Dantas, N.O. Raman spectroscopy of very small $Cd_{1-x}Co_xS$ quantum dots grown by a novel protocol: direct observation of acoustic-optical phonon coupling. J. Raman Spectrosc. **2013**, *44*, 1022-1032, doi:10.1002/jrs.4324.

[43] Ardit, M.; Dondi, M.; Cruciani, G.; Zanelli, C. Tetrahedrally coordinated Co2+in oxides and silicates: Effect of local environment on optical properties. Am. Mineral. **2014**, *99*, 1736-1745, doi:10.2138/am.2014.4877.

[44] Tanabe, Y.; Sugano, S. On the Absorption Spectra of Complex Ions. J. Phys. Soc. Japan **1954**, *9*, 753-766, doi:10.1143/JPSJ.9.753.